Research Square

Preprints are preliminary reports that have not undergone peer review.
They should not be considered conclusive, used to inform clinical practice,
or referenced by the media as validated information.

Integrated Single-Cell and Spatial Transcriptome Analysis Reveals the Biological Characteristics and Regulatory Mechanisms of Atypical Epithelium in Solid-Type Adenoid Cystic Carcinoma

Xiaotian Yuan
Xiangya Hospital of Central South University
Lai Meng
Xiangya Hospital of Central South University
Linwei Wu
Xiangya Hospital of Central South University
Yan Fang
Tianjin Medical University Cancer Institute and Hospital
Dongge Li
Xiangya Hospital of Central South University
Zirong Chen
Xiangya Hospital of Central South University
Benjian Zhang
Guangxi Medical University Cancer Hospital
Yunqing Liu
Xiangya Third Hospital of Central South University
Yaxuan Wang
Xiangya Hospital of Central South University
Yongzhen Mo
Xiangya Hospital of Central South University
Zhouying Peng
Xiangya Hospital of Central South University
Hua Zhang
Xiangya Hospital of Central South University
Weihong Jiang
jiangwh68@126.com

Xiangya Hospital of Central South University

Article

Keywords: Adenoid cystic carcinoma, solid-type, heterogeneity, non-classical epithelial cell

Posted Date: September 9th, 2026

DOI: https://doi.org/10.21203/rs.3.rs-10204394/v1

License: This work is licensed under a Creative Commons Attribution 4.0 International License.
Read Full License

Additional Declarations: No competing interests reported.

Abstract

(1) Background:

Solid-type adenoid cystic carcinoma (ACC) is a highly invasive and heterogeneous tumor, but the molecular heterogeneity and malignant transformation mechanisms have not been clearly investigated.

(2) Methods:

Single-cell RNA sequencing (scRNA-seq) and spatial transcriptomics (ST) were employed to identify characteristic tumor cell subpopulations in solid-type ACC, which were then validated in tissue samples. Functional experiments were conducted to explore the regulatory mechanisms of malignant transformation.

(3) Results:

ACC exhibited two non-classical epithelial cell subpopulations with rapid proliferation and dedifferentiation characteristics. The non-classical epithelial marker keratin 81 (KRT81) can serve as a molecular typing marker for solid-type ACC, with its protein expression significantly higher in solid-type tissues compared to non-solid types. In vitro and in vivo experiments demonstrated that non-classical epithelial cells promoted the formation of malignant phenotype by activating epithelial-mesenchymal transition (EMT) and cell cycle progression through the MESP1/MACC1 axis. Moreover, non-classical epithelial cells can also induce tumor immune evasion by secreting migration inhibitory factor (MIF) to promote M2 macrophage polarization.

(4) Conclusion:

Non-classical epithelial cells represent a characteristic cellular subpopulation in solid-type ACC. MESP1/MACC1 and MIF serve as core regulatory factors in tumor cell dedifferentiation and immune evasion. These findings provide new molecular targets to overcome the current treatment challenges in solid-type ACC.

Introduction

Adenoid cystic carcinoma (ACC) is a rare malignancy originating from salivary glands and other exocrine glands, accounting for 1%-2% of head and neck malignancies[1]. Its hallmark pathological features include biphasic differentiation of ductal epithelial and myoepithelial cells, forming tubular, cribriform, or solid architectural patterns[2]. Among these subtypes, solid-type ACC exhibits poor clinical prognosis, with a 5-year survival rate below 50%, due to the absence of classic cribriform structures, marked cellular

atypia, and high proliferative activity[1]. Although surgery combined with radiotherapy remains the primary treatment, advanced patients often lack effective therapeutic options due to distant metastasis (e.g., lung, bone) or local recurrence[3]. Therefore, unraveling the tumor heterogeneity and malignant transformation mechanisms of solid-type ACC is critical for improving diagnosis and treatment.

Recent advances in molecular characterization of ACC have identified key drivers. Whole-genome sequencing reveals MYB-NFIB fusion genes in 50%-70% of ACC cases, which promote tumor cell survival by activating MYB target genes (e.g., BCL2, KIT)[4]. Additionally, dysregulation of NOTCH signaling, TP53 mutations, and PI3K/AKT/mTOR pathway aberrations are implicated in ACC progression[5]. However, these findings predominantly derive from bulk tissue analyses, obscuring intratumoral cellular heterogeneity. Single-cell RNA sequencing (scRNA-seq) has emerged as a powerful tool to dissect ACC cellular composition. For instance, recent studies identified tumor cell subpopulations with stem-like properties in ACC, characterized by high expression of SOX4 and ALDH1A1, potentially linked to chemoresistance[6]. Nevertheless, whether solid-type ACC harbors distinct pro-malignant subpopulations and how their molecular networks drive aggressive proliferation and invasion remain unresolved.

The aggressiveness of solid-type ACC may stem from altered cellular differentiation states. In multiple solid tumors, tumor cell dedifferentiation—marked by loss of epithelial markers (e.g., E-cadherin), upregulation of mesenchymal markers (e.g., Vimentin), and activation of proliferation-associated genes (e.g., MKI67)—is a central event in malignant transformation[7]. This process is often mediated by transcription factors (e.g., TWIST1, SNAIL) driving epithelial-mesenchymal transition (EMT)[7]. Furthermore, dysregulated cell cycle control (e.g., overexpression of E2F family members) disrupts G1/S phase transition, fueling rapid tumor proliferation[8].

Based on this background, this study integrates scRNA-seq, spatial transcriptomics (ST), and functional assays to systematically dissect tumor heterogeneity in solid-type ACC and elucidate regulatory mechanisms underlying its malignant phenotype. Key scientific questions include: (1) Does solid-type ACC harbor distinct tumor cell subpopulations absent in non-solid subtypes? (2) Do these subpopulations drive dedifferentiation and hyperproliferation via specific transcriptional networks? (3) Can clinically actionable molecular markers be identified for diagnosis or therapeutic intervention?

Materials and methods

Acquisition and Preprocessing of scRNA-seq Data

The scRNA-seq dataset utilized in this study was obtained from the in-house sequencing database of the research group[9]. Library preparation was performed using the 10x Genomics Chromium Single Cell 3’ Library Kit. Sequencing was conducted on the Illumina NovaSeq 6000 platform. Raw FASTQ files were processed with CellRanger software to align reads to the human reference genome (GRCh38) and generate a gene expression matrix. Quality control was implemented in the R environment using the

Seurat package, with the following criteria: (1) retention of genes detected in at least three cells; (2) exclusion of cells expressing fewer than 300 or more than 3,000 genes; (3) removal of cells with mitochondrial gene content exceeding 10% of total reads; and (4) elimination of cells with total read counts surpassing 10,000. Batch effects and technical noise were corrected using the SCTransform function in Seurat. Cell cycle variation was regressed out based on cell cycle scores computed by the CellCycleScoring function. Doublets were identified and removed using the DoubletFinder tool, leveraging the top 20 principal components from PCA and an expected doublet rate derived from the Chromium Single-Cell 3' v2 reagents kit guidelines (10X Genomics). For downstream analysis, 3,000 highly variable genes (HVGs) were selected for PCA, followed by batch effect correction of principal components using the Harmony algorithm. Cell clusters were identified via the K-nearest neighbors (KNN) algorithm, and differentially expressed genes (DEGs) across clusters were determined using the Wilcoxon rank-sum test. Genes with adjusted p-values < 0.05 and absolute log2 fold change ≥ 0.5 were defined as cluster-specific marker genes. These markers were annotated using the CellMarker online database for cell type identification.

Acquisition and Preprocessing of ST Data

The spatial transcriptomics (ST) dataset was retrieved from the research group's sequencing database[9]. Fresh adrenocortical carcinoma (ACC) tissues were cryopreserved, embedded, and processed according to the 10x Genomics protocol. Libraries were constructed using the Visium Spatial Gene Expression Kit and sequenced on the Illumina NovaSeq 6000 platform. Post-sequencing, raw reads underwent quality filtering and were aligned to the human genome (GRCh38) via STAR within the SpaceRanger software. Tissue capture regions were visualized using image processing algorithms, and spatial expression matrices were generated. Normalization of expression matrices was performed using the SCTransform function in Seurat. Normalized matrices and spatial coordinates were imported into Loupe software for gene expression visualization and spatial domain segmentation.

Cell Developmental Trajectory Analysis

Pseudotemporal trajectory inference was conducted using Monocle2 to delineate dynamic cell state transitions. Normalized gene expression matrices and cell metadata were extracted from Seurat objects and converted into a CellDataSet object via the newCellDataSet function. Data normalization and dispersion estimation were executed using estimateSizeFactors and estimateDispersions. Trajectory construction employed 3,000 HVGs selected by setOrderingFilter. Nonlinear dimensionality reduction was performed using reduceDimension (max_components = 2, norm_method = "log") to project cells into a low-dimensional manifold. Root nodes were manually defined based on biological priors via orderCells. Pseudotemporal trajectories were visualized in two dimensions using plot_cell_trajectory.

Gene Set Enrichment Analysis

Gene Ontology Biological Process (GO-BP) enrichment analysis was performed in R using the clusterProfiler package. A pre-ranked gene list sorted by log2 fold change was input into the GSEA function. GO-BP gene sets were retrieved from the msigdbr package, with gene identifiers converted to Entrez IDs. Significantly enriched pathways (adjusted $p < 0.05$) were filtered, and the top 10 pathways ranked by absolute normalized enrichment score (NES) were visualized via dot plots.

Transcription Factor Activity Analysis

SCENIC (v1.3.1) was implemented in R to infer transcription factor (TF) regulatory networks. Normalized expression matrices from Seurat were integrated with the hg19-tss-centered-10kb-7species.mc9nr.feather database for motif annotation. SCENIC parameters were initialized with the human genome. The workflow included: (1) co-expression network construction via runGenie3; (2) regulon inference using runSCENIC_2_createRegulons; (3) motif validation and regulon activity scoring (AUCell) via runSCENIC_3_scoreCells; and (4) binarization of regulon activity states using runSCENIC_4_aucell_binarize. Output matrices (AUCmatrix: 3.4_regulonAUC.Rds; BINmatrix: 4.1_binaryRegulonActivity.Rds) were analyzed for TF activity dynamics and integrated with functional annotations.

Cell–Cell Communication Analysis

Cell–cell communication analysis was conducted using the CellChat package in R. ScRNA-seq data from epithelial cells were first integrated, and a CellChat object was created using the normalized expression matrix and cell identity labels. The human ligand–receptor interaction database provided by CellChat was used as the reference. The functions identifyOverExpressedGenes and identifyOverExpressedInteractions were applied to identify significantly overexpressed ligand–receptor pairs. To enhance prediction accuracy, the interactions were further mapped onto a protein–protein interaction network using the projectData function. During inference of the communication network, intercellular communication probabilities were computed using the computeCommunProb function, and low-confidence interactions were filtered out. Pathway-level communication was then inferred with the computeCommunProbPathway function, and significant pathway interactions were extracted. A heatmap of pathway-level communication was visualized using the netVisual_heatmap function.

Clinical Sample Collection

The collection of human tissues and tumor samples was approved by the Ethics Committee of Xiangya Hospital, Central South University (Approval No. 202408159, August 2024). We confirm that all methods were performed in accordance with the relevant guidelines and regulations. Furthermore, all research involving human participants was conducted in strict accordance with the Declaration of Helsinki. Informed consent was obtained from all participants and/or their legal guardians. Specimens for histopathology and protein analysis were fixed in 10% neutral buffered formalin, while those for nucleic

acid studies were preserved in RNA stabilization solution and stored at -80℃. The cohort included 3 solid and 5 non-solid samples for scRNA-seq, 1 solid and 1 non-solid sample for ST, and 3 solid and 3 non-solid validation samples.

Hematoxylin and Eosin (H&E) Staining

Tissues fixed in 10% formalin for 12–24 hours were dehydrated through graded ethanol (70%-100%), cleared in xylene, and paraffin-embedded. Sections (5 μm) were dewaxed in xylene, rehydrated in ethanol gradients, stained with hematoxylin (5 min) and eosin (30 sec), dehydrated, cleared, and mounted with neutral resin for microscopic analysis.

Tissue Immunofluorescence Staining

Paraffin-embedded sections were dewaxed, rehydrated, and subjected to antigen retrieval in Tris-EDTA buffer (95℃, 20 min). After blocking with 20% BSA (30 min, RT), sections were incubated with primary antibodies (4℃, overnight) and fluorescent secondary antibodies (1 hour, RT), followed by DAPI counterstaining. Images were captured using a slide scanner and analyzed with CaseViewer/ImageJ. The following antibodies were used in this study: Anti-KRT81 (Proteintech, China);Anti-pan-CK (Proteintech, China); Anti-CD206 (Proteintech, China)Anti-CD68 (Proteintech, China).

Western Blot (WB)

Cells were lysed in RIPA buffer (4℃, 15 min), centrifuged (12,000 rpm, 15 min), and quantified via BCA assay. Proteins (30 μg/lane) were separated by 10% SDS-PAGE, transferred to PVDF membranes, and probed with primary (4℃, overnight) and HRP-conjugated secondary antibodies (1 hour, RT). Bands were visualized using ECL and analyzed with ImageJ. Primary Antibodies: Anti-MKI67 (Proteintech, China); Anti-GAPDH (Proteintech, China); Anti-MACC1 (Abcam, USA); Anti-MESP1 (Affinity, China); Anti-N-cadherin (Proteintech, China); Anti-Vimentin (Proteintech, China). Secondary Antibodies: HRP-conjugated Goat Anti-Rabbit IgG(H + L) (Proteintech, China); HRP-conjugated Goat Anti-Mouse IgG(H + L) (Proteintech, China).

RT-qPCR

RNA extracted with Trizol was reverse-transcribed using SweScript RT II Kit. qPCR was performed with Fast SYBR Green Master Mix. Cycling conditions: 95℃ (30 sec), 40 cycles of 95℃ (10 sec), 60℃ (30 sec). Relative expression was calculated via $2^{-\Delta\Delta Ct}$ method (GAPDH-normalized). Primer sequences: MACC1 (Forward: CCCGGGTTTGGTAGAGTGAC; Reverse: GGAAGTGAGCCCAAGCTTCT); IL10 (Forward: GGGCACCCAGTCTGAGAA; Reverse: GCAACCCAGGTAACCCTTAAAGT); MRC1 (Forward: GTGATGGGACCCCTGTAACG; Reverse: CTGCCCAGTACCCATCCTTG); GAPDH (Forward: GGGGCTCTCCAGAACATC; Reverse: TGACACGTTGGCAGTGG).

Primary Cell Isolation and Purification

Freshly resected ACC tissues were minced into small fragments and digested in 1 mg/mL collagenase type I at 37℃ with gentle agitation for 1 hour. The resulting cell suspension was filtered through a 40 μm cell strainer to remove undigested tissue fragments. The filtered cells were washed with PBS, resuspended in a specialized primary ACC culture medium, and seeded into 6-well plates. Cells were incubated for 48 hours, during which non-adherent cells were removed periodically. The specialized primary ACC culture medium consisted of serum-free Advanced DMEM/F12 supplemented with 10 μM Y-27632, 1 mM N-acetylcysteine, 10 μM nicotinamide, 50 ng/mL epidermal growth factor (EGF), 100 ng/mL fibroblast growth factor 10 (FGF10), 100 ng/mL R-spondin1, 50 ng/mL Noggin, and FibrOut™ fibroblast inhibitor (CHI SCIENTIFIC, China). After 48 hours of culture in the specialized medium, when the cells reached approximately 80% confluence, the medium was replaced with RPMI-1640 supplemented with 10% fetal bovine serum (FBS) and cells were further cultured for 24 hours. The supernatant was then collected for subsequent experiments. A small fraction of the primary cells was retained for immunofluorescence staining to confirm the epithelial identity and ensure that fibroblast contamination was below 0.1%.

Tumor Cell Culture and Cell Behavior Experiments

STR-validated SACC-83 cells were cultured in DMEM supplemented with 10% FBS and antibiotics at 37℃ under 5% CO2, passaged with 0.25% trypsin at 80% confluence; for functional assays: (1) Colony Formation: 500 cells/well were seeded in 6-well plates, cultured for 14 days, fixed with 4% paraformaldehyde, stained with 0.1% crystal violet, and colonies (> 50 cells) counted via ImageJ; (2) Cell Invasion: 5×105 cells/mL in serum-free medium were added to Matrigel-coated Transwell chambers, incubated for 24 hours, and invaded cells on the lower membrane were fixed, stained, and quantified; (3) Wound Healing: Confluent monolayers were scratched with a pipette tip, washed, and cultured in serum-free medium, with migration rates calculated at 0/24/48 hours using ImageJ via the formula: Migration rate (%) = [(Initial width − Time-point width)/Initial width] × 100%.

THP-1 Cell Culture and Macrophage Induction

STR-authenticated THP-1 cells were cultured in RPMI-1640 medium supplemented with 10% fetal bovine serum (FBS) and a reducing agent. Prior to experimental treatments, THP-1 cells were stimulated with 100 ng/ml phorbol 12-myristate 13-acetate (PMA) for 24 hours to induce differentiation from a monocytic state into adherent, unactivated macrophages (M0 phenotype). After PMA induction, the medium was removed and replaced with conditioned medium for an additional 72-hour incubation. For inhibitor experiments, ISO-1 (10 μM) was added during the conditioning phase.

Immunofluorescence Staining

Cells were first washed three times with PBS to remove the culture medium. They were then fixed with 4% paraformaldehyde at room temperature for 20 minutes, followed by three additional PBS washes. To block nonspecific binding, cells were incubated with 2.5% bovine serum albumin (BSA) at room temperature for 1 hour. After blocking, cells were washed three times with PBST (PBS containing 0.1% Tween-20). Primary antibodies diluted in blocking buffer were added and incubated overnight at 4°C. The

next day, the primary antibody solution was removed and cells were washed three times with PBST. Secondary antibodies diluted in blocking buffer were then added and incubated at room temperature for 1 hour in the dark. Afterward, cells were washed three times with PBST. Nuclei were counterstained with DAPI for 5 minutes at room temperature, followed by three PBST washes. Finally, cells were mounted with anti-fade mounting medium and visualized under a fluorescence microscope. The following antibodies were used in this study: Anti-Vimentin (Proteintech, China);Anti-pan-CK (Proteintech, China)

Plasmid Construction & Amplification

The MESP1 CDS was cloned into the pLenti-GIII-CMV-3xFlag-Puro vector downstream of the CMV promoter for overexpression. For MACC1 knockdown, a shRNA (CTCAGAGGTAAGATTGGACTT) was inserted into the pLenti-U6-shRNA-Puro vector. DH5α E.coli competent cells were transformed via ice incubation (20 minutes), 42℃ heat shock (45 seconds), ice recovery (2–3 minutes), and 1-hour LB medium shaking (37℃). Transformed cells were plated on ampicillin-LB agar (38℃, 12 hours), and single colonies were expanded in ampicillin/kanamycin-LB liquid medium (37℃, 12 hours). Plasmid DNA was extracted using the GoldHi EndoFree Kit, eluted in endotoxin-free TE buffer, quantified (A260/A280: 1.8–2.0), aliquoted, and stored at − 20°C.

Lentiviral Packaging and Transduction

293T cells at 80% confluency were cultured in DMEM basal medium. Solution A (Lipofectamine 3000/Opti-MEM) and Solution B (10 μg target plasmid, 4 μg pMD2.G, 6 μg psPAX2, P3000/Opti-MEM) were incubated separately for 5 minutes, combined, and incubated for 20 minutes. The mixture was added to 293T cells; after 8-hour transfection, the medium was replaced with complete DMEM. Viral supernatant was collected 24 hours post-transfection. SACC-83 cells (40% confluency) were transduced with viral supernatant for 48 hours, followed by 48-hour puromycin selection (2 μg/mL) to eliminate untransduced cells. GFP expression (> 90% cells) was confirmed via fluorescence microscopy. Stable polyclonal populations were established through repeated puromycin screening. Transduction efficiency was validated by Western blot for target protein expression.

ELISA

The concentration of MIF was quantified using a standardized commercial ELISA kit. Standards and test samples were added to the antibody-coated wells and incubated at room temperature for 120 minutes. Following washing steps, biotinylated detection antibody working solution was added and incubated for 60 minutes at room temperature. The enzyme conjugate working solution was then added and incubated for 20 minutes under light-protected conditions at room temperature. After color development with TMB substrate, the optical density of each well was measured at 450 nm. Between each step, the plates were washed three times with PBS containing 0.05% Tween-20.

Animal Experiments

Animal experiments were approved by the Animal Ethics Committee of Central South University (Approval No. CSU-2024-0145), and all methods were performed in accordance with the relevant

guidelines and regulations. Additionally, the study was reported in compliance with the ARRIVE guidelines. SACC-83 cells in the logarithmic growth phase were digested with 0.25% trypsin, centrifuged, resuspended in PBS, and adjusted to 2×10^7 cells/mL. A 100 µL cell suspension was subcutaneously injected into the right axilla of 6-week-old BALB/c-nu nude mice (Animals were obtained from Shanghai Model Organisms Center, Inc). Tumor length and width were measured on days 7, 14, and 21 post-injection. On day 21, mice were humanely euthanized via carbon dioxide (CO_2) inhalation in a dedicated displacement chamber, with a gradual CO_2 flow rate displacing 20% of the chamber volume per minute. Death was confirmed by the permanent cessation of respiration and cardiac arrest, followed by cervical dislocation as a secondary physical method to ensure death, consistent with the AVMA Guidelines for the Euthanasia of Animals (2020). Tumor tissues were excised and weighed. Tumor volume was calculated as Volume = 0.5 × length × width^2.

Statistical Analysis

Statistical analyses and visualization were performed using R language and GraphPad Prism 10. The ggplot2 and ggsignif packages were employed for hypothesis testing and mean/median comparisons, while heatmap generation and hierarchical clustering utilized the pheatmap package with default algorithms. Statistical tests included: t-tests for independent samples (normal distribution, homoscedasticity), Wilcoxon rank-sum tests for non-normal data, and paired t-tests for paired samples. Multiple group comparisons were assessed by one-way ANOVA followed by SNK-Q tests for pairwise analysis. Statistical significance was defined as $p < 0.05$ (*), $p < 0.01$ (**), $p < 0.001$ (***), and $p < 0.0001$ (****).

Results

A Distinct Tumor Cell Subpopulation in Solid-Type ACC Exhibits High Proliferative Capacity and Dedifferentiation Features

ScRNA-seq was performed on tumor samples from eight ACC patients who underwent surgical resection, including three cases each of solid-type and cribriform-type, and two cases of tubular-type ACC. Clustering, annotation, and inference of malignant cells were conducted based on methods previously published by our group[9, 10]. Malignant cells were extracted for further analysis. Secondary clustering of tumor cells revealed heterogeneity within ACC (Fig. 1A, B). Given the biphasic differentiation of ACC into ductal and myoepithelial lineages, along with a subset exhibiting high-grade transformation and increased proliferative capacity, lineage-specific markers were employed to classify epithelial subtypes. Ductal epithelial clusters (Due1–Due4) were characterized by high expression of glandular markers (KRT7, KRT8, KRT18, MUC1, and MUC4), while myoepithelial clusters (Me1–Me2) expressed myogenic markers (ACTA2, TAGLN, MYH11, and TPM2), consistent with classical ACC features.

In addition, two non-classical epithelial subpopulations were identified: dedifferentiated epithelium (Dee) and proliferating epithelium (Pe), both exhibiting markedly reduced expression of ductal and myoepithelial markers. Dee showed mildly elevated expression of proliferation-associated genes (MKI67, CDK1, CCNE1, PCNA, and TOP2A), whereas Pe displayed strong upregulation of these genes (Fig. 1A). When comparing tumor cell subpopulation distributions across histological subtypes (Fig. 1C–E), these two non-classical subtypes were predominantly enriched in solid-type ACC. Although ductal and myoepithelial cells remained the major components in solid-type ACC, the proportion of non-classical epithelial cells was significantly higher than in non-solid types (Fig. 1D).

Pseudotime analysis showed that Dee and Pe converged at the same terminal differentiation state, suggesting a shared differentiation trajectory (Fig. 1F). Differential expression analysis between non-classical and classical epithelial subsets revealed unique gene signatures in Dee and Pe (Fig. 1G, H), which were subjected to pathway enrichment analysis (Fig. 1I, J). Both non-classical subpopulations exhibited activation of DNA replication, mismatch repair, cell cycle, and oxidative phosphorylation pathways, indicative of high proliferative and metabolic activity. Conversely, pathways associated with differentiation, such as actin cytoskeleton regulation, smooth muscle contraction, and focal adhesion, were downregulated. Notably, KRT81 was significantly upregulated in both Dee and Pe clusters (Fig. 1G, H).

KRT81 Serves as a Marker for Non-Classical Epithelial Cells in Solid-Type ACC

KRT81 was found to be highly expressed in both non-classical epithelial subtypes based on scRNA-seq data (Fig. 1G, H), but was nearly absent in classical epithelial populations (Fig. 2A). ST data revealed that KRT81 and MKI67 were both strongly expressed and spatially co-localized in solid-type ACC, while their expression was minimal in non-solid-type ACC (Fig. 2B, C). Immunofluorescence staining further confirmed that a significantly higher proportion of pan-CK-positive epithelial cells expressed KRT81 in solid-type compared to non-solid-type ACC (Fig. 2D). Western blot analysis also demonstrated markedly elevated KRT81 protein levels in solid-type ACC tissues (Fig. 2E, F).

MESP1 Drives the Malignant Phenotype of Non-Classical Epithelial Cells

To investigate regulatory mechanisms underlying non-classical epithelial phenotypes, we performed single-cell transcription factor activity analysis using SCENIC. Differential regulon activity analysis revealed distinct transcription factor modules among tumor cell subpopulations (Fig. 3A). Hierarchical clustering based on transcription factor signatures indicated similar regulatory profiles between Pe and Dee clusters, with both showing strong activation of the MESP1 regulon. In addition, proliferation-associated transcription factors such as E2F1, E2F7, and BRCA1 were specifically activated in the Pe cluster (Fig. 3A). These findings suggest that MESP1 may act as a key driver of the transition from

classical to non-classical epithelial phenotypes, while activation of E2F and BRCA1 modules may further promote proliferative behavior.

Analysis of SCENIC-predicted MESP1 targets identified a core binding motif (CAGGTG), which is present upstream (430–436 bp) of the transcription start site of MACC1 (Metastasis-Associated in Colon Cancer 1), suggesting that MESP1 may directly regulate MACC1 expression (Fig. 3B, C). To validate this, we established MESP1-overexpressing SACC-83 cell lines and examined the expression of MESP1, MACC1, and EMT markers (Fig. 3D). MESP1 overexpression led to upregulation of MACC1, N-cadherin, and Vimentin. Functionally, MESP1 overexpression enhanced clonogenicity (Fig. 3E, F), wound healing capacity (Fig. 3G, H), and invasion through Matrigel (Fig. 3I, J), indicating acquisition of EMT and increased malignancy consistent with features of non-classical epithelial cells in solid-type ACC.

MESP1 Promotes the Malignant Phenotype Through Transcriptional Activation of MACC1

To further confirm that MESP1 regulates malignant behavior via MACC1, we generated MACC1-knockdown cells on the MESP1-overexpressing background. RT-qPCR and western blot showed reduced expression of MACC1, N-cadherin, and Vimentin following knockdown (Fig. 4A, B). Colony formation, migration, and invasion assays demonstrated that MACC1 knockdown significantly impaired these malignant traits (Fig. 4C–H). In vivo, subcutaneous implantation of SACC-83 wild-type, MESP1-overexpressing, and MESP1-overexpressing/MACC1-knockdown cells into nude mice showed that tumors from the latter group were smaller in size and weight compared to the MESP1-only group, though slightly larger than the wild-type (Fig. 4I–K), confirming that MESP1 promotes the malignant phenotype in part via MACC1 upregulation.

Non-Classical Epithelial Cells Promote Immune Evasion by Inducing M2 Polarization via MIF Secretion

Cell–cell communication analysis revealed that MIF signaling between non-classical epithelial clusters (Pe and Dee) and immune cells—particularly myeloid, B, and T/NK cells—was markedly enriched compared to classical epithelial subtypes (Fig. 5A–C), with MIF−(CD74 + CD44) and MIF−(CD74 + CXCR4) being the predominant ligand–receptor interactions. Signal origin analysis showed that epithelial cells were the primary sources of MIF, while immune cells were major recipients, and immune cells themselves exhibited low levels of MIF autocrine signaling (Fig. 5D). Among immune cell populations, myeloid cells were the main targets of epithelial-derived MIF (Fig. 5E). Given that MIF is a known inducer of M2 macrophage polarization, we assessed M2 marker expression in ACC tissues. CD68 + macrophages in solid-type ACC exhibited significantly higher expression of CD206 compared to non-solid types (Fig. 6A, B). Given that MIF is a known inducer of M2 macrophage polarization, we evaluated the expression of M2 markers in ACC tissues. Compared to non-solid ACC, solid ACC exhibited significantly higher CD206 expression in $CD68^{+}$ macrophages (Figs. 6A, B). Cellular immunofluorescence revealed that pan-CK-positive epithelial cells in solid ACC showed markedly increased vimentin co-

expression relative to non-solid ACC (Fig. 6C). ELISA further demonstrated upregulated MIF secretion in solid versus non-solid ACC (Fig. 6D). Immunofluorescence analysis confirmed that MIF stimulation induced M2 marker expression in macrophages, while co-treatment with the MIF antagonist ISO-1 abolished this effect (Fig. 6E). Consistent with these findings, RT-qPCR showed that MIF upregulated both IL-10 and MRC1 expression in macrophages, which was similarly suppressed by ISO-1 (Figs. 6F, G).

Discussion

ACC is a malignant salivary gland tumor with heterogeneous characteristics, and its pathological subtypes (solid and non-solid) are significantly associated with clinical prognosis[11, 12]. This study revealed two characteristic tumor cell subpopulations in solid-type ACC using scRNA-seq technology, namely dedifferentiated epithelium and proliferating epithelium. These subpopulations showed partial loss of the classic ACC differentiation features of glandular epithelium (KRT7/KRT18+) and myoepithelium (ACTA2/MYH11+), as well as significant proliferating activity. Temporal expression analysis showed that the two non-classical epithelia were distributed at the same differentiation endpoint, suggesting that they may originate from identical progenitor cell or complete malignant transformation through a common differentiation pathway. This finding provides a explanation for the high invasiveness of solid-type ACC at a cellular level.

As for the molecular pathways, non-classical epithelial subpopulations significantly activated DNA replication, mismatch repair, and oxidative phosphorylation, which were consistent with the clinical feature of high Ki-67 index in solid-type ACC. Notably, the inhibition of pathways such as actin cytoskeleton regulation and focal adhesion may weaken intercellular junctions and polarity maintenance, leading to the detachment of tumor cell from primary site and enhancing invasive ability[13, 14]. This “high proliferation and low differentiation” molecular phenotype may be closely related to the rapid progression and early metastasis of solid-type ACC. ST analysis showed the colocalization of KRT81 and MKI67 in solid-type ACC, suggesting that KRT81 + cells may form a proliferating environment through paracrine or autocrine mechanisms, further accelerating tumor malignant transformation. This study firstly proposed that KRT81 could serve as a specific marker gene for non-classical epithelium. KRT81 belongs to the type II keratin family, and previous studies mainly focused on its expression regulation in squamous cell carcinoma[15]. In the present study, it had a unique spatial distribution characteristic in ACC. Immunofluorescence staining showed that pan-CK positive cells in solid-type ACC highly expressed KRT81, and the protein level was significantly higher than that in non-solid ACC. Members of the keratin family typically participate in the maintenance of cytoskeletal stability[16]. The high expression of KRT81 in ACC may have a dual role: on the one hand, the upregulation may reflect the reconstruction of the keratin network during the dedifferentiation process of tumor cells; on the other hand, KRT81 may indirectly promote proliferation by activating the PI3K/AKT or WNT pathways. Future studies need to verify the function of KRT81 in ACC through gene knockout experiments and explore its synergistic effects with therapeutic targets such as EGFR and HER2.

In this study, the transcription factor MESP1 and its regulatory module were activated in solid-type ACC. MESP1 is known to regulate cardiac progenitor cell differentiation and EMT during embryonic development[17, 18], but its function in tumors remains unclear. This study discovered that the MESP1 module was specifically activated in dedifferentiated and proliferating epithelium, and its binding motif (CAGGTG) was located in the MACC1 promoter region. By constructing MESP1 overexpression cell lines, it was confirmed that MESP1 could upregulate MACC1 expression, induce EMT phenomenon (upregulation of N-cadherin and Vimentin), and enhancing cell clone formation, migration, and invasion abilities. The results suggested that MESP1 may drive the malignant transformation of tumor cells by reprogramming their differentiation state.

MACC1 was firstly discovered in colorectal cancer and associated with increased tuor metastasis, cell survival, proliferation, and migration[19]. Subsequently, MACC1 was found to be involved in the formation and migration of various solid tumors, including glioblastoma[20], ovarian cancer[21], gastric cancer[22], hepatocellular carcinoma[23], and others[24]. Many upstream and downstream targets of MACC1 have been identified and are associated with typical tumor characteristics, such as regulating OCT4 to induce tumor cell dedifferentiation, and regulating VEGF and TWIST1/2 to participate in angiogenesis[25]. This study found that MACC1 was directly regulated by MESP1 in ACC, and its expression level was positively correlated with the EMT process. After knocking down MACC1, the migration and invasion abilities of MESP1 overexpression strain were significantly decreased, indicating that MACC1 was a core effector molecule downstream of MESP1. In addition, cell drived xenograft tumor resuls showed that the activation of MESP1/MACC1 significantly promoted tumor growth. Apart from MESP1, the activation of transcription factor modules such as E2F1, E2F7, and BRCA1 in proliferating epithelium further amplified the malignant phenotype. Members of the E2F family promote cell cycle progression by regulating the G1/S phase transition[26, 27]. The deficiency of BRCA1 often leads to genomic instability[28]. In solid-type ACC, MESP1 may maintain the continuous proliferation and invasive ability of tumor cells through synergistic interactions with transcription factors such as E2F and BRCA.

Additionally, this study further explored the interaction mechanisms between non-classical epithelial cells and immune cells, revealing that macrophage migration inhibitory factor (MIF) played a pivotal role in cellular interactions. This study identified that in ACC, MIF was predominantly secreted by epithelial cells and acted on immune cells via its corresponding receptors. Solid-type ACC exhibited significantly upregulated MIF secretion compared to non-solid ACC. As a crucial immunomodulatory factor, MIF contributes to the progression of various inflammatory diseases and tumors by promoting M2 macrophage polarization[29, 30]. Previous research has demonstrated elevated MIF expression in solid-type tumors, such as prostate cancer[31], melanoma[32], and hepatocellular carcinoma[33], where high M2 macrophage infiltration is strongly correlated with enhanced tumor aggressiveness and poor prognosis. This study provides evidence that macrophage MIF promotes M2 macrophage polarization, concomitant with upregulation of the characteristic M2 markers IL-10 and MRC1. Previous studies demonstrating that $MRC1^+$ macrophages and IL-10 secretion contribute significantly to the development of an immunosuppressive tumor microenvironment, particularly through their roles in inhibiting antitumor

immunity and promoting tumor progression[34, 35]. Overall, epithelial-derived MIF in ACC facilitates the formation of an immunosuppressive tumor microenvironment by promoting M2 macrophage polarization. Further exploration of the mechanism of MIF action is expected to provide novel targeted therapeutic strategies for ACC.

In summary, this study has potential clinical translational value. The combination of KRT81 and MKI67 can serve as a molecular typing marker for solid-type ACC, aid in rapid diagnosis through frozen sections or needle biopsies, and indicate the potential for non-solid ACC to transform into solid ACC. Small molecule inhibitors of the MESP1/MACC1 pathway (such as MACC1 antagonist ND-654) may inhibit the EMT process. E2F inhibitors (such as HLM006474) may reverse abnormal cell cycle activation. Therapeutic agents targeting MIF signaling pathways (such as bufalin) represent promising candidates for novel ACC treatment strategies.

Declarations

Funding

This research was funded by the The Science & Technology Development Fund of Tianjin Education Commission（No. 2023KJ094）.

Competing Interests

The authors have no relevant financial or non-financial interests to disclose.

Clinical trial number

Not applicable.

Author Contributions

Xiaotian Yuan, Hua Zhang, Weihong Jiang: conceived and designed the experiments; Xiaotian Yuan, Lai Meng, Linwei Wu: performed the experiments; Zirong Chen, Yunqing Liu, Yaxuan Wang, Zhouying Peng: analyzed and interpreted the data; Yongzhen Mo, Zhouying Peng, Hua Zhang, Weihong Jiang: contributed reagents, materials, analysis tools or data; Xiaotian Yuan, Lai Meng, Linwei Wu, Dongge Li: wrote the paper. Yan Fang provided the sequencing data.

Data Availability

The single-cell (GSE342688, secure token: ghurcggqfpqfxyh) and spatial transcriptome (GSE342687, secure token: etcfuqssplkbtid) sequencing data of adenoid cystic carcinoma (ACC) generated in this study have been deposited in the Gene Expression Omnibus (GEO).

Ethics approval

Tissue sampling was conducted following the guidelines of the International Organization of Medical Sciences and the World Health Organization and was approved by the Xiangya hospital Research Ethics Committee of the Central South University (approval number: No. 202408159). Animal experiments were approved by the Animal Ethics Committee of Central South University (approval number: CSU-2024-0145).

Consent to participate

Written informed consent was obtained from the parents.

Consent to publish

The authors affirm that human research participants provided informed consent for publication of the images

Acknowledgements

Not applicable

References

1. COCA-PELAZ A, RODRIGO J P, BRADLEY P, J. et al. Adenoid cystic carcinoma of the head and neck–An update [J]. *Oral Oncol.* **51** (7), 652–661 (2015).
2. SEETHALA, R. R. & STENMAN, G. Update from the 4th Edition of the World Health Organization Classification of Head and Neck Tumours: Tumors of the Salivary Gland [J]. *Head Neck Pathol.* **11** (1), 55–67 (2017).
3. DILLON, P. M. et al. Adenoid cystic carcinoma: A review of recent advances, molecular targets, and clinical trials [J]. *Head Neck*. **38** (4), 620–627 (2016).
4. PERSSON, M. et al. Recurrent fusion of MYB and NFIB transcription factor genes in carcinomas of the breast and head and neck [J]. *Proc. Natl. Acad. Sci. U S A*. **106** (44), 18740–18744 (2009).
5. POWELL, S. K. & KULAKOVA, K. KENNEDY S. A Review of the Molecular Landscape of Adenoid Cystic Carcinoma of the Lacrimal Gland [J]. *Int. J. Mol. Sci.*, **24**(18). (2023).
6. FERRAROTTO, R. et al. Proteogenomic Analysis of Salivary Adenoid Cystic Carcinomas Defines Molecular Subtypes and Identifies Therapeutic Targets [J]. *Clin. Cancer Res.* **27** (3), 852–864 (2021).
7. DONGRE, A. & WEINBERG, R. A. New insights into the mechanisms of epithelial-mesenchymal transition and implications for cancer [J]. *Nat. Rev. Mol. Cell. Biol.* **20** (2), 69–84 (2019).
8. KENT L N. The broken cycle: E2F dysfunction in cancer [J]. *Nat. Rev. Cancer*. **19** (6), 326–338 (2019).
9. FANG, Y. et al. Improvements and challenges of tissue preparation for spatial transcriptome analysis of skull base tumors [J]. *Heliyon* **9** (3), e14133 (2023).
10. YUAN, X. et al. Combining single-cell spatial transcriptomics and molecular simulation to develop in vivo probes targeting the perineural invasion region of adenoid cystic carcinoma [J]. *Heliyon* **10** (15),

e34628 (2024).

11. WANG, Y. et al. Genetic heterogeneity and therapeutic target detection through microdissection in solid-type adenoid cystic carcinoma [J]. *Pathology* **54** (5), 580–590 (2022).
12. ZHANG, Y. et al. Notch activation leads to loss of myoepithelial differentiation and poor outcome in solid adenoid cystic carcinoma [J]. *Oral Dis.* **26** (8), 1677–1686 (2020).
13. DONG, Y. et al. CLDN6 inhibits breast cancer metastasis through WIP-dependent actin cytoskeleton-mediated autophagy [J]. *J. Exp. Clin. Cancer Res.* **42** (1), 68 (2023).
14. CHASTNEY M R, KAIVOLA, J. et al. The role and regulation of integrins in cell migration and invasion [J]. *Nat. Rev. Mol. Cell. Biol.* **26** (2), 147–167 (2025).
15. MENG, D. et al. Screening the key genes of prognostic value in the microenvironment for head and neck squamous cell carcinoma [J]. *Med. (Baltim).* **100** (4), e24184 (2021).
16. MOCH, M. & LEUBE, R. E. SRC and ERK Regulate the Turnover of Cytoskeletal Keratin Filaments [J]. *Int. J. Mol. Sci.*, **26**(12). (2025).
17. KRUP A L, WINCHESTER S A B, RANADE, S. S. et al. A Mesp1-dependent developmental breakpoint in transcriptional and epigenomic specification of early cardiac precursors [J]. *Development*, **150**(9). (2023).
18. LINDSLEY R C et al. Mesp1 coordinately regulates cardiovascular fate restriction and epithelial-mesenchymal transition in differentiating ESCs [J]. *Cell. Stem Cell.* **3** (1), 55–68 (2008).
19. STEIN, U. et al. MACC1, a newly identified key regulator of HGF-MET signaling, predicts colon cancer metastasis [J]. *Nat. Med.* **15** (1), 59–67 (2009).
20. HOHMANN, T. et al. MACC1 driven alterations in cellular biomechanics facilitate cell motility in glioblastoma [J]. *Cell. Commun. Signal.* **18** (1), 85 (2020).
21. SCHWARZ F M, K. U. H. L. M. A. N. N. J. D. et al. Induction of circulating ABCB1 transcripts under platinum-based chemotherapy indicates poor prognosis and a bone micrometastatic phenotype in ovarian cancer patients [J]. *Mol. Cancer*. **23** (1), 174 (2024).
22. TREESE, C. et al. Inhibition of MACC1-Induced Metastasis in Esophageal and Gastric Adenocarcinomas [J]. *Cancers (Basel)*, **14**(7). (2022).
23. WAN, T. et al. LncRNA DDX11-AS1 accelerates hepatocellular carcinoma progression via the miR-195-5p/MACC1 pathway [J]. *Ann. Hepatol.* **20**, 100258 (2021).
24. LV, M. et al. MACC1 as a Potential Target for the Treatment and Prevention of Breast Cancer [J]. *Biology (Basel)*, **12**(3). (2023).
25. LEMOS C, HARDT M S, JUNEJA, M. et al. MACC1 Induces Tumor Progression in Transgenic Mice and Colorectal Cancer Patients via Increased Pluripotency Markers Nanog and Oct4 [J]. *Clin. Cancer Res.* **22** (11), 2812–2824 (2016).
26. KASSAB, A. & GUPTA I, MOUSTAFA, A. A. Role of E2F transcription factor in oral cancer: Recent insight and advancements [J]. *Semin Cancer Biol.* **92**, 28–41 (2023).

27. SUN, M. et al. Posttranslational modifications of E2F family members in the physiological state and in cancer: Roles, mechanisms and therapeutic targets [J]. *Biomed. Pharmacother*. **178**, 117147 (2024).
28. YOSHIDA, K. & MIKI, Y. Role of BRCA1 and BRCA2 as regulators of DNA repair, transcription, and cell cycle in response to DNA damage [J]. *Cancer Sci.* **95** (11), 866–871 (2004).
29. BOZZA M T, L. I. N. T. O. M. E. N. L. et al. The Role of MIF on Eosinophil Biology and Eosinophilic Inflammation [J]. *Clin. Rev. Allergy Immunol.* **58** (1), 15–24 (2020).
30. XU, X. I. A. O. S. M. et al. Gastrointestinal stromal tumors regulate macrophage M2 polarization through the MIF/CXCR4 axis to immune escape [J]. *Front. Immunol.* **15**, 1431535 (2024).
31. CAO, T. et al. EAF2 Downregulation Recruits Tumor-associated Macrophages in Prostate Cancer through Upregulation of MIF [J]. *Biol. Proced. Online*. **26** (1), 21 (2024).
32. TANESE, K. & OGATA, D. The role of macrophage migration inhibitory factor family and CD74 in the pathogenesis of melanoma [J]. *Exp. Dermatol.* **33** (6), e15122 (2024).
33. ZHU, G. Q. et al. CD36(+) cancer-associated fibroblasts provide immunosuppressive microenvironment for hepatocellular carcinoma via secretion of macrophage migration inhibitory factor [J]. *Cell. Discov*. **9** (1), 25 (2023).
34. WU, Z. Unveiling the Impact of MRC1 on Immune Infiltration and Patient's Prognosis: A Pan-Cancer Analysis Based on Single-Cell and Bulk Sequencing [J]. *Int. J. Gen. Med.* **17**, 2575–2592 (2024).
35. LIU, Q. et al. Wnt5a-induced M2 polarization of tumor-associated macrophages via IL-10 promotes colorectal cancer progression [J]. *Cell. Commun. Signal.* **18** (1), 51 (2020).

Figures

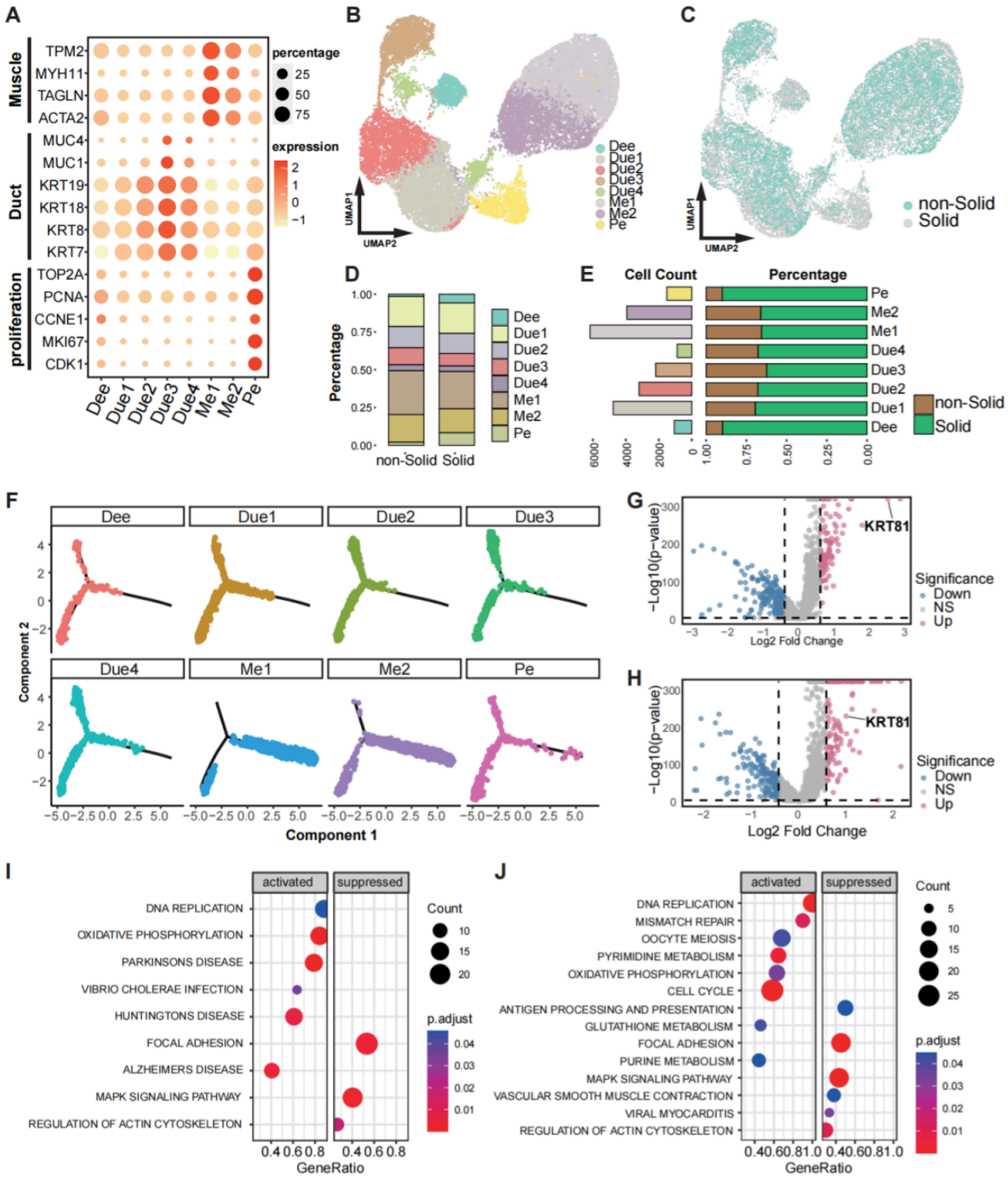
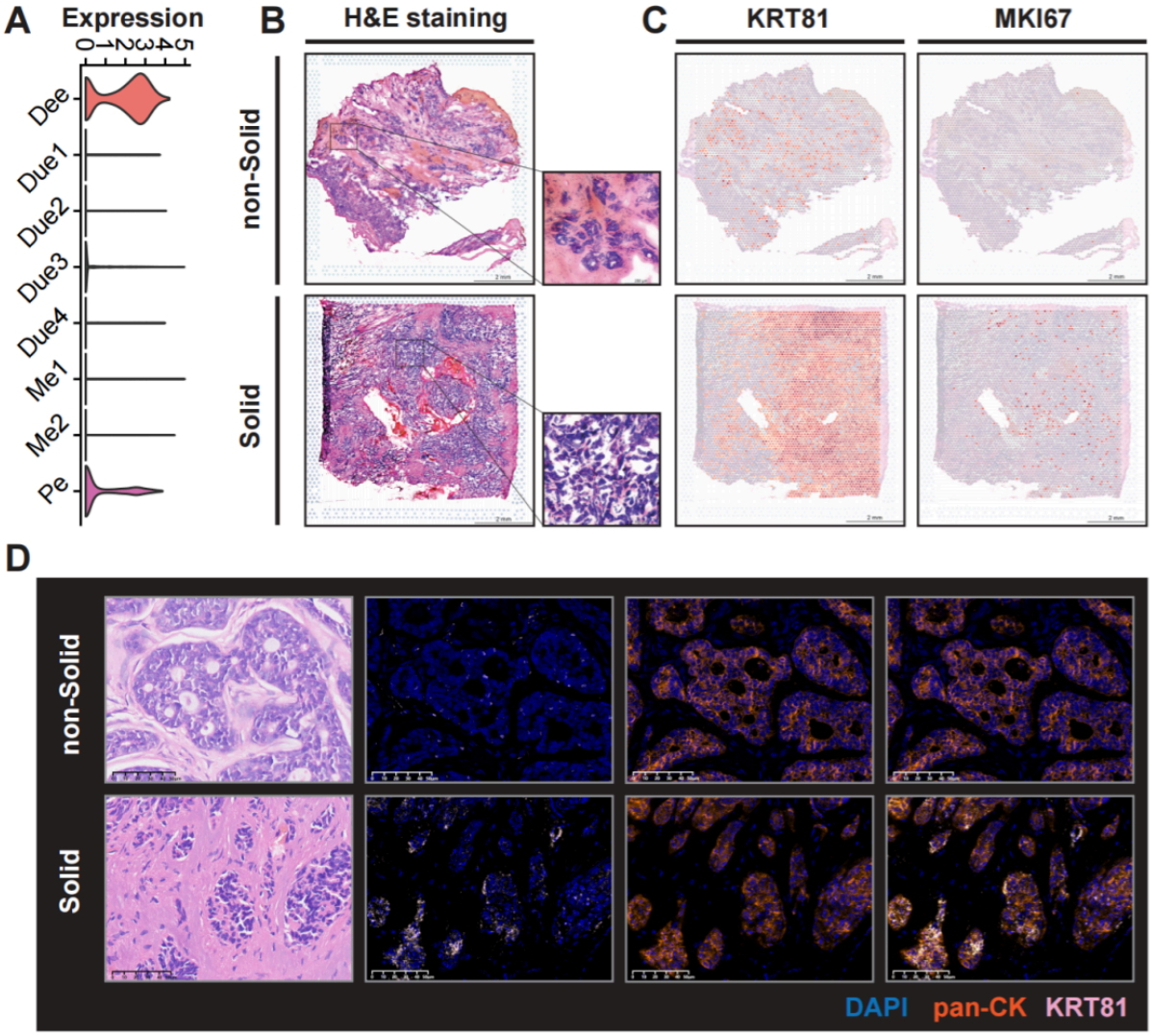
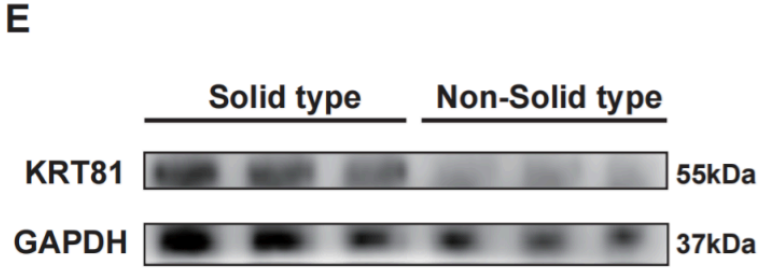


Figure 1

Single-cell transcriptional profiling of ACC tumor cells. (A) Bubble plot displays marker gene expression across distinct tumor cell subpopulations, with color intensity representing expression levels and bubble size indicating the proportion of expressing cells. **(B)-(C)** UMAP visualization of the two-dimensional distribution of transcriptional profiles in tumor cells, where colors denote either cell subpopulations or pathological subtypes. **(D)** Stacked bar plot illustrates the proportional composition of tumor cell

subpopulations stratified by pathological subtype. **(E)** Bar plot quantifies cell abundance and tissue origin across tumor cell subtypes. **(F)** Pseudotime trajectory analysis reveals divergent differentiation endpoints among tumor cell subpopulations. **(G)-(H)** Volcano plots highlight differentially expressed genes when comparing Dee (G) and Pe (H) against classical epithelial cells. KRT81 is significantly upregulated in both non-classical epithelial subtypes. **(I)-(J)** Enrichment analysis of differentially expressed genes from Dee (I) and Pe (J). Activated and suppressed pathways are labeled accordingly.





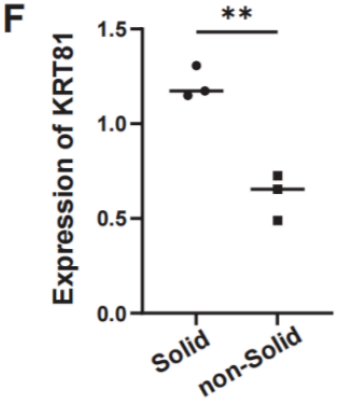


Figure 2

Expression of KRT81 in different subtypes of ACC. (A) Violin plot depicting KRT81 expression across distinct epithelial subtypes in scRNA-seq data. **(B)-(C)** Tissue H&E staining and spatial expression of KRT81 and MKI67 of ST sequencing samples. **(D)** Immunofluorescence staining demonstrating protein expression of pan-CK and KRT81 in non-Solid and Solid ACC subtypes. **(E)-(F)** Western blot analysis of KRT81 protein levels in 3 Solid and 3 non-Solid ACC cases. Significance: **, P<0.01.

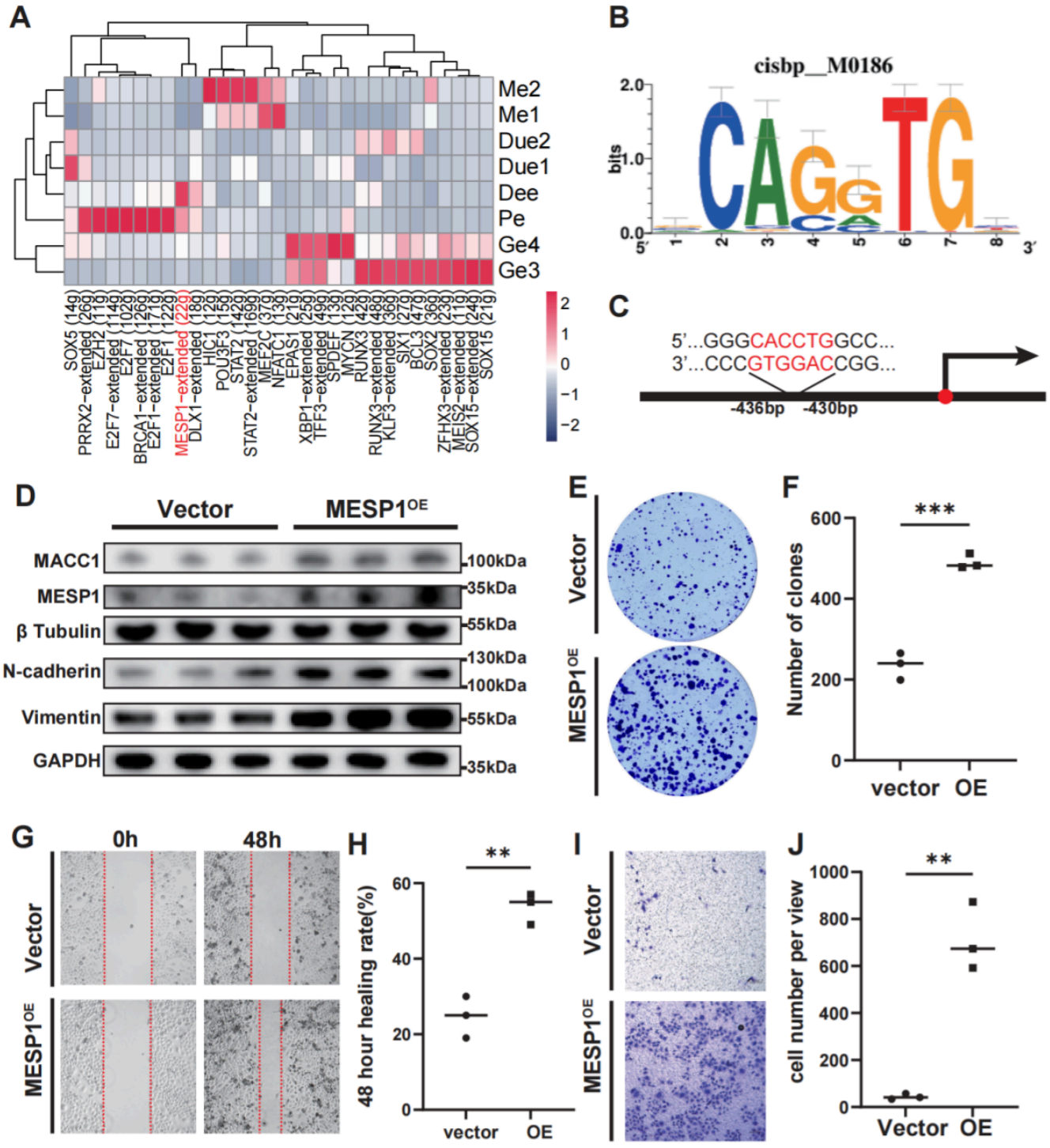


Figure 3

Expression of transcription factor MESP1 and its impact on ACC tumor cell behavior. (A) Heatmap displaying expression levels of differentially expressed transcription factor modules across ACC subpopulations, with hierarchical clustering of both cell subpopulations and transcription factor modules based on expression levels. **(B)** Sequence logo plot of the MESP1 binding motif in upstream regions of target genes, with the X-axis indicating nucleotide position and the Y-axis representing conservation frequency. **(C)** Presence of MESP1 binding motif in the upstream regulatory region of the MACC1 transcription start site. **(D)** Western blot analysis of protein expression levels in empty vector-transfected and MESP1-overexpressing (OE) SACC-83 cell lines. **(E)-(F)** Colony formation assay comparing the two cell lines. Significance: ***, P<0.001. **(G)-(H)**Wound healing assay comparing the two cell lines. Significance: **, P<0.01. **(I)-(J)** Cell invasion assay comparing the two cell lines. Significance: **, P<0.01.

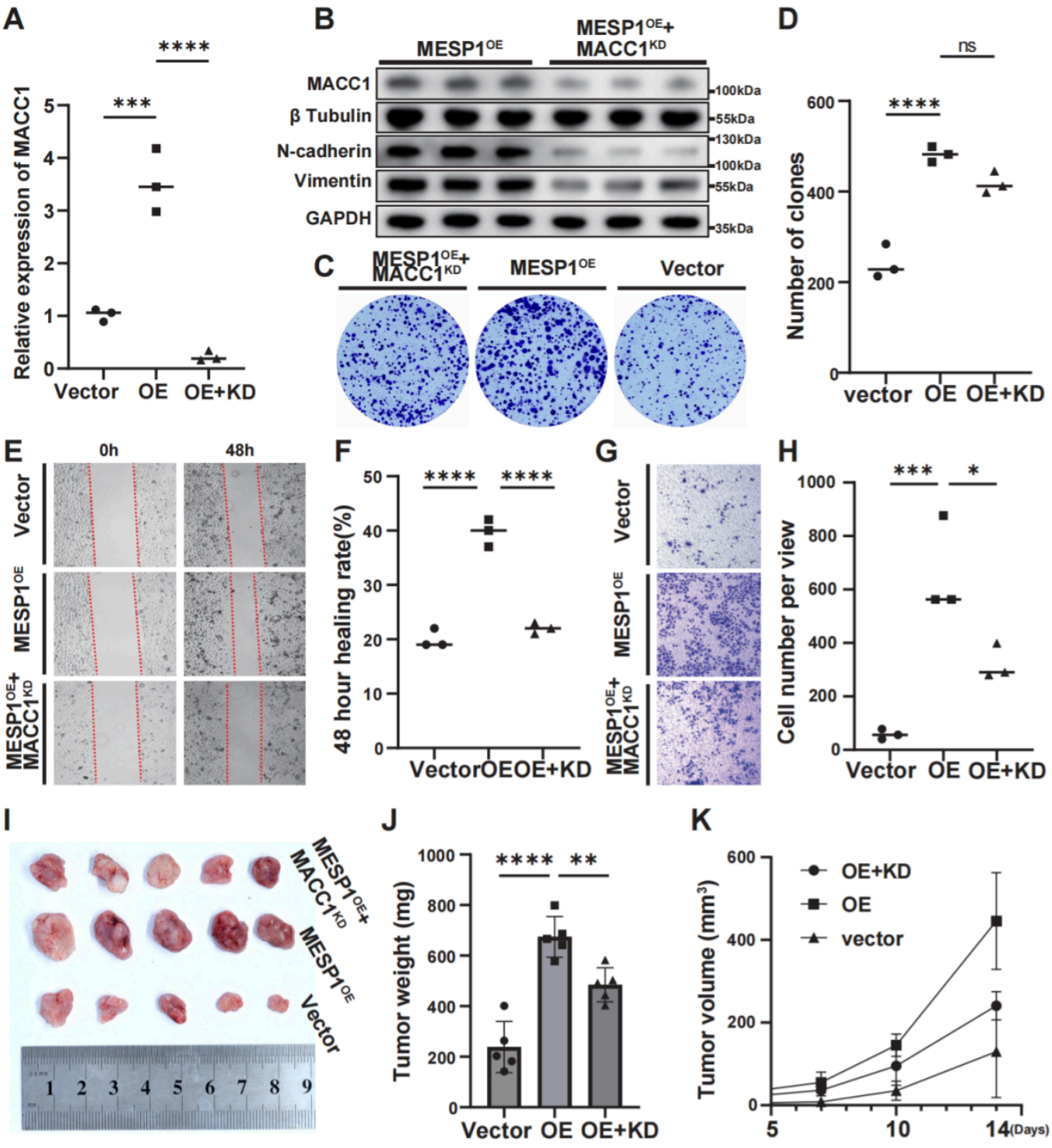


Figure 4

MESP1 regulates ACC tumor cell behavior through transcriptional control of MACC1. (A) MACC1 mRNA expression levels in SACC-83 cells transfected with empty vector, MESP1-overexpressing (OE), and MESP1-overexpressing/MACC1-knockdown (OE+KD) constructs. Significance: ***, P<0.001; ****, P<0.0001. **(B)** Western blot analysis of protein expression levels in the three transfected cell lines. **(C)-(D)** Colony formation assay of the three transfected cell lines. Significance: ****, P<0.0001; ns, P≥0.05.

(E)-(F) Wound healing assay of the three cell transfected lines. Significance: ****, P<0.0001. **(G)-(H)** Transwell invasion assay of the three transfected cell lines. Significance: ***, P<0.001; *, P<0.05. **(I)-(K)** Xenograft tumor models showing representative images (I), tumor weight (J), and growth curves (K) derived from the three transfected cell lines. Significance: ****, P<0.0001; **, P<0.01.

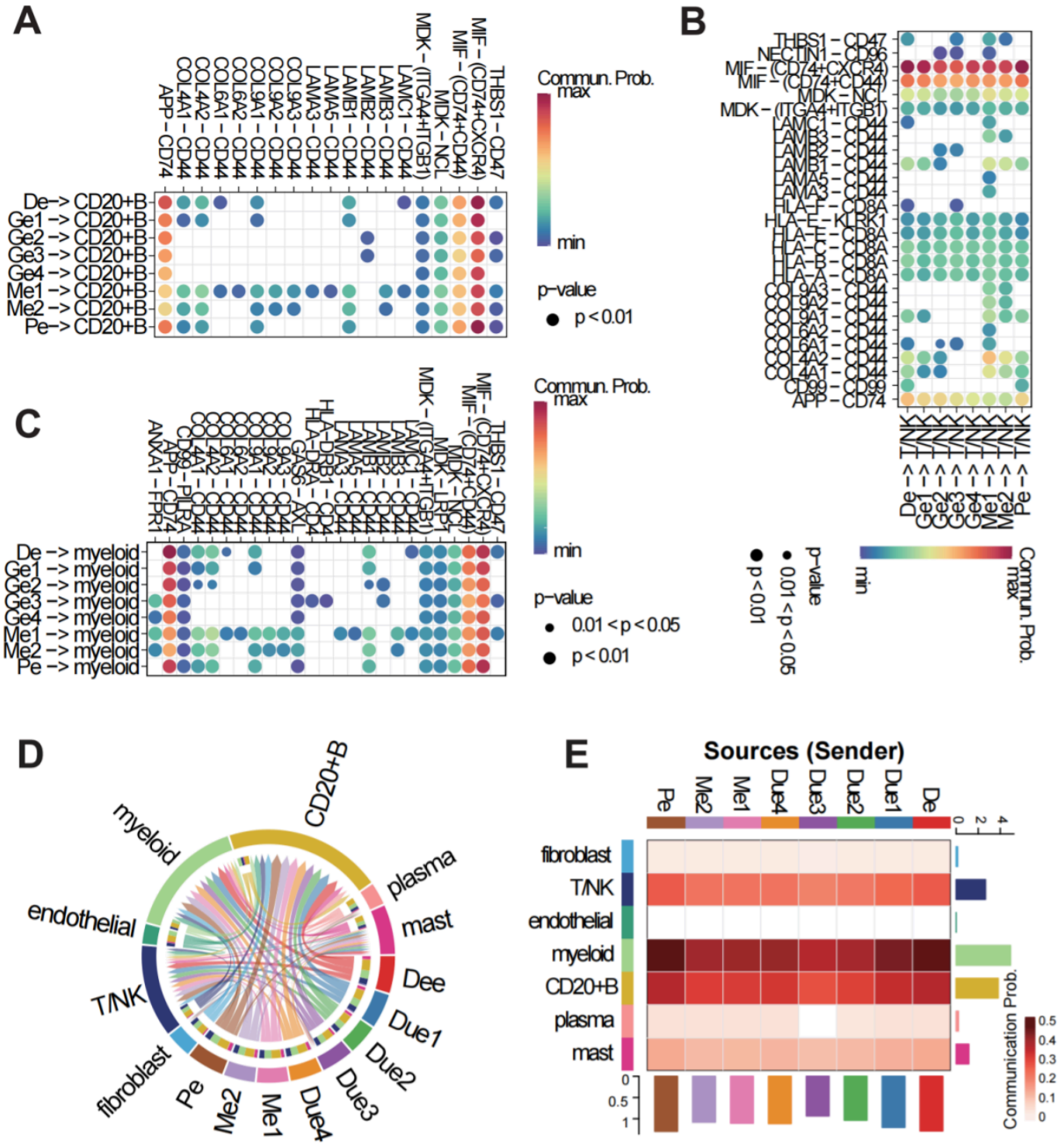


Figure 5

Cell–cell Communication Between non-classical epithelial clusters (Pe and Dee) and immune cells in ACC. (A-C) Bubble plots display receptor-ligand pairs mediating interactions between ACC epithelial subtypes and B cells (A), T/NK cells (B), and myeloid cells (C). Bubble size represents statistical significance, while color intensity indicates relative interaction strength. **(D)** Circos plot analyzes MIF signaling networks across cell subpopulations, with thicker connecting lines denoting stronger cellular crosstalk. **(E)** Heatmap depicts MIF-mediated interactions between epithelial subpopulations and other cell types, while color intensity indicates relative interaction strength.

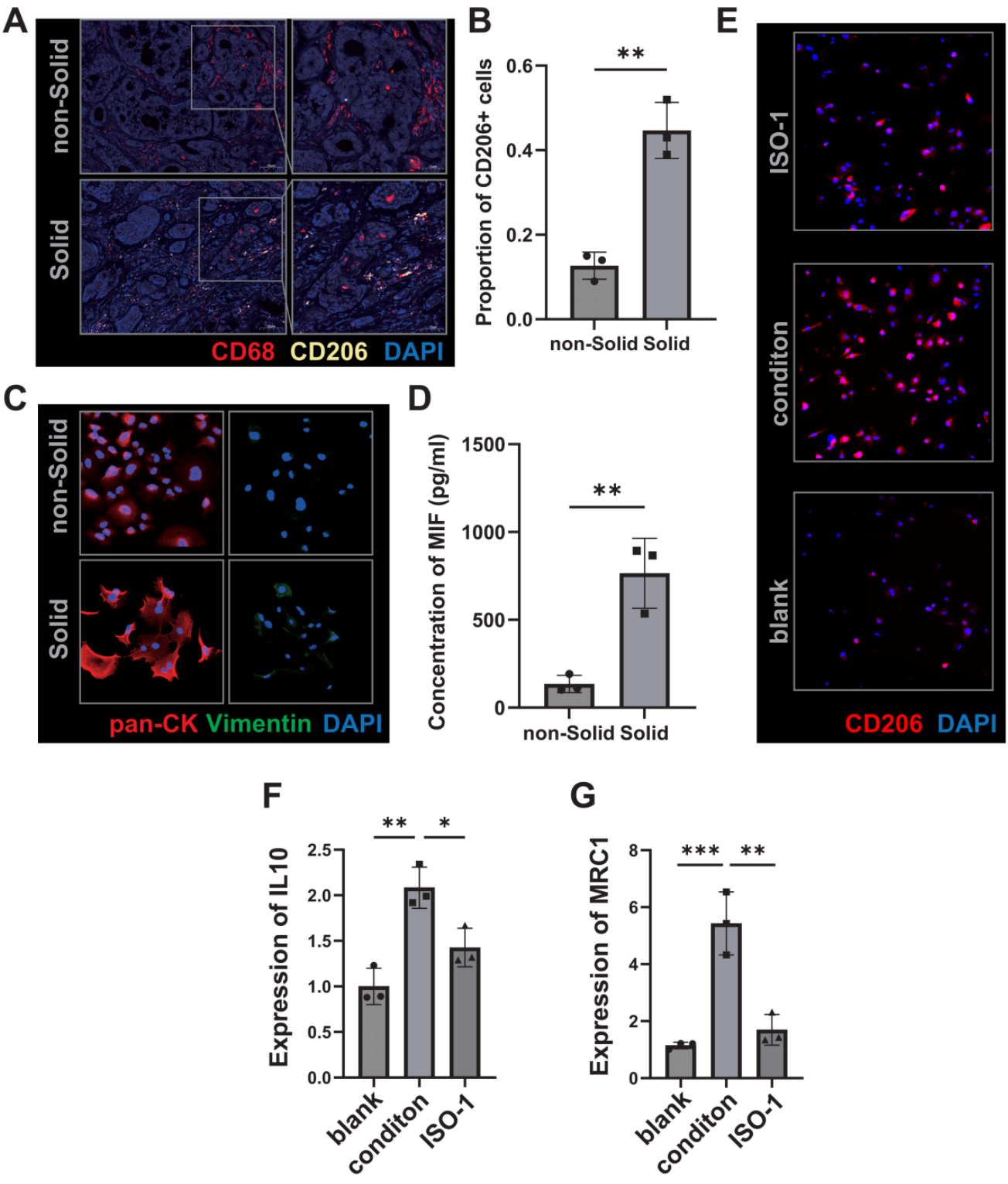


Figure 6

MIF modulates tumor immune microenvironment by regulating M2 macrophage polarization. (A-B) Immunofluorescence staining of tumor tissues demonstrates CD206 protein expression in non-solid and solid ACC subtypes. **(C)** Cellular immunofluorescence reveals protein expression of pan-CK and vimentin in non-solid and solid ACC cells. **(D)** ELISA quantifies secreted MIF levels in non-solid and solid ACC media. **(E)** Immunofluorescence analysis of $CD206^{+}$ macrophages treated with MIF alone, or MIF plus ISO-1. **(F-G)** RT-qPCR analysis demonstrates relative mRNA expression levels of M2 macrophage polarization markers IL-10 and MRC1 in macrophages treated with MIF alone, or MIF plus ISO-1.

Supplementary Files

This is a list of supplementary files associated with this preprint. Click to download.

- supplementaryfiles1.pdf